High-resolution room-temperature sample scanning superconducting quantum interference device microscope configurable for geological and biomagnetic applications

L. E. Fong, J. R. Holzer, K. K. McBride, E. A. Lima, and F. Baudenbacher[a]
Vanderbilt University, Nashville, Tennessee 37235

M. Radparvar
Hypres Inc., Elmsford, New York 10523

We have developed a scanning superconducting quantum interference device (SQUID) microscope system with interchangeable sensor configurations for imaging magnetic fields of room-temperature (RT) samples with submillimeter resolution. The low-critical-temperature (T_c) niobium-based monolithic SQUID sensors are mounted on the tip of a sapphire and thermally anchored to the helium reservoir. A 25 μm sapphire window separates the vacuum space from the RT sample. A positioning mechanism allows us to adjust the sample-to-sensor spacing from the top of the Dewar. We achieved a sensor-to-sample spacing of 100 μm, which could be maintained for periods of up to four weeks. Different SQUID sensor designs are necessary to achieve the best combination of spatial resolution and field sensitivity for a given source configuration. For imaging thin sections of geological samples, we used a custom-designed monolithic low-T_c niobium bare SQUID sensor, with an effective diameter of 80 μm, and achieved a field sensitivity of 1.5 pT/Hz$^{1/2}$ and a magnetic moment sensitivity of 5.4×10^{-18} A m^2/Hz$^{1/2}$ at a sensor-to-sample spacing of 100 μm in the white noise region for frequencies above 100 Hz. Imaging action currents in cardiac tissue requires a higher field sensitivity, which can only be achieved by compromising spatial resolution. We developed a monolithic low-T_c niobium multiloop SQUID sensor, with sensor sizes ranging from 250 μm to 1 mm, and achieved sensitivities of 480–180 fT/Hz$^{1/2}$ in the white noise region for frequencies above 100 Hz, respectively. For all sensor configurations, the spatial resolution was comparable to the effective diameter and limited by the sensor-to-sample spacing. Spatial registration allowed us to compare high-resolution images of magnetic fields associated with action currents and optical recordings of transmembrane potentials to study the bidomain nature of cardiac tissue or to match petrography to magnetic field maps in thin sections of geological samples. © *2005 American Institute of Physics.* [DOI: 10.1063/1.1884025]

I. INTRODUCTION

Room-temperature (RT) sample scanning superconducting quantum interference device (SQUID) microscopy (SSM) is a very powerful and promising technique for imaging magnetic field distributions.[1,2] In addition to the SQUID's unsurpassed field sensitivity, this technique is completely non-invasive and can be implemented to study a great variety of samples. RT sample SSM is continuing to play an important role in biomagnetism,[3–8] nondestructive evaluation,[9–14] and geomagnetism.[15,16]

Since the field and spatial resolution are highly diminished as the distance between the sample and the sensor increases, the key to this technique is to bring the sensor, held at cryogenic temperatures, as close as possible to the sample. It has been shown that the best combination of spatial resolution and field sensitivity for a specific SQUID geometry occurs when the diameter of the pickup coil is approximately equal to the sample-to-sensor distance.[17]

A SQUID sensor measures the integrated magnetic flux over the sensing area. Thus, the SQUID's sensitivity to magnetic fields scales as $1/a^2$, where a is the diameter of the sensing area. The fall-off rate of the magnetic field depends on the type of source. For a current-carrying wire the field scales as $1/r$, and for a magnetic dipole it scales as $1/r^3$, where r is the distance from the source. The best combination of field sensitivity and spatial resolution requires $a = r$. It is easy to show that the signal-to-noise ratio of fields generated by a current-carrying wire is proportional to a, and for a magnetic dipole, proportional to $1/a$. Therefore, we have to use different strategies to optimize the sensor geometry and the sample-to-sensor distance depending on the application. In geomagnetism we are dealing with magnetic dipoles, while biomagnetic signals are typically generated by either axial currents or sheets of current.

In this article, we describe a high-resolution SQUID imaging system that can be configured either with monolithic low-T_c directly coupled single-turn SQUIDs, multiloop SQUIDs, or miniature pickup coils inductively coupled to commercial low-T_c SQUIDs, as sensing elements for differ-

---

[a]Electronic mail: F.Baudenbacher@Vanderbilt.edu

ent applications. The system is highly stable, user friendly, and cost efficient. The system versatility is demonstrated by presenting data on high-resolution magnetic imaging of geological thin sections and magnetic mapping of action current distributions in cardiac tissue.

II. SCANNING SQUID MICROSCOPE SYSTEM DESIGN

In the following sections, we present various designs for directly coupled monolithic SQUID sensors, targeting spatial resolutions ranging from 50 μm to 1 mm, their device characteristics, and their incorporation into our SQUID microscope. We also describe a positioning mechanism that allows the cryogenic sensors to be positioned within 10 μm of a RT sapphire window, and our Dewar design that allows operation of the SQUID microscope with a helium consumption of 1.0 l/day.

A. Directly coupled monolithic SQUID sensors

Our first generation of SQUID microscopes used hand-wound superconducting niobium-wire miniature pickup coils connected directly to the terminals of a flux transformer circuit of commercially available low-T_c SQUID sensors.[18] With this configuration, we achieved field sensitivities, for frequencies above 1 Hz, of 850 fT/Hz$^{1/2}$ and 330 fT/Hz$^{1/2}$, using a 10-turn 250 μm diameter and a 20-turn 500 μm diameter pickup coil, respectively. However, the miniature pickup coil configuration has two major drawbacks in accomplishing the optimum combination of field sensitivity and spatial resolution. The first limitation is the impedance mismatch between the pickup coil and the flux transformer circuit. For optimum coupling and, therefore, the best possible magnetic field sensitivity, the flux transformer input coil and the pickup coil impedances must be the same. Commercially available low-T_c SQUID sensors typically have input coil impedances on the order of 2 μH, which is 20 times higher than the impedance of a 20-turn 500 μm pickup coil. Impedance matching is increasingly difficult as we reduce the pickup coil size and is impractical for spatial resolutions below 250 μm. The second limitation is the spatial integration of the magnetic field over the volume of the pickup coil. For example, a 20-turn double-layer cylindrical coil wound with a 25 μm wire has a minimal height of 250 μm. The taller the pickup coil, the less magnetic flux each turn collects, since the magnetic field decays as we increase the distance from the sample. This integration generally compromises the spatial resolution but leads to a higher field sensitivity. However, in terms of sensitivity to dipole moments, a better signal-to-noise ratio can be achieved if a small coil is brought closer to the sample.[19] In this case, the limiting factor is generally the distance between the sample and the SQUID sensor.

To overcome these drawbacks, we developed different types of thin-film monolithic low-T_c niobium SQUID sensors, which measure the magnetic field coupled directly into the self-inductance of the SQUID. In the first type of sensor, a single SQUID washer acts as the sensing area. A detailed layout and an equivalent circuit of this design are shown in Fig. 1. In this approach, the sensing area is a two-
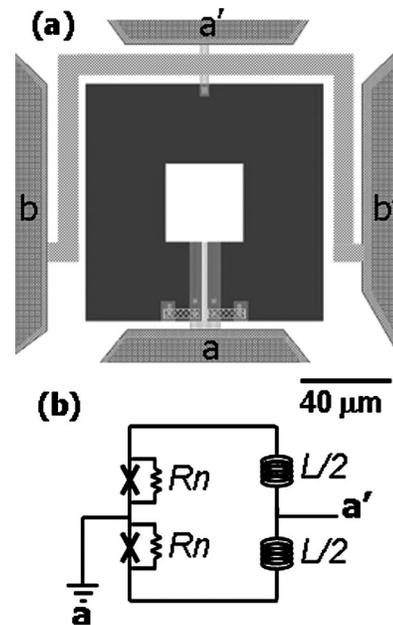

FIG. 1. (a) Layout of our bare SQUID design. The SQUID terminals are labeled a and a' and the contact pads for the feedback coil b and b'. (b) Equivalent electric circuit diagram of the bare SQUID. R_n is the shunt resistance in parallel with the Josephson junctions and L is the inductance of the device.

dimensional plane rather than a volume, as in the case of the miniature hand-wound pickup coils. The noise performance of an optimized SQUID sensor is limited by its inductance and is described by the power spectral density of the equivalent flux noise:[20]

$$S_\phi(f) = \frac{16k_B T L^2}{R_n},\tag{1}$$

where f denotes the frequency, k_B the Boltzmann constant, T the operational temperature, R_n the shunt resistance, and L the inductance of the device. The main contribution to the inductance is determined by the sensor size.[21] Therefore, the intrinsic noise of the bare SQUID increases with its geometrical size, so that this approach cannot be scaled up to sensor diameters larger than 250 μm.[22]

Using a bare SQUID with a 40 μm hole and a 120 μm square washer, we achieved a flux noise of 4 $\mu\phi_0$/Hz$^{1/2}$, where ϕ_0 is the magnetic flux quantum, and an equivalent field sensitivity of 1.5 pT/Hz$^{1/2}$ in the white noise region for frequencies above 100 Hz. The bare SQUID design is particularly suited for localized source configurations wherein the signal decreases rapidly with distance, as is the case for dipolar sources. As we mentioned before, the size of the SQUID washer should be chosen to be comparable to the sensor-to-sample distance for optimum tradeoff between spatial resolution and field sensitivity. The use of the bare SQUID for a RT-sample SSM is suited for spatial resolutions on the order of tens of micrometers to 250 μm.

For imaging applications in which higher field sensitivities are required, we have to compromise spatial resolution in order to achieve larger effective areas. This is especially true in the case of imaging weak magnetic fields generated by distributed action currents associated with bioelectric phe-
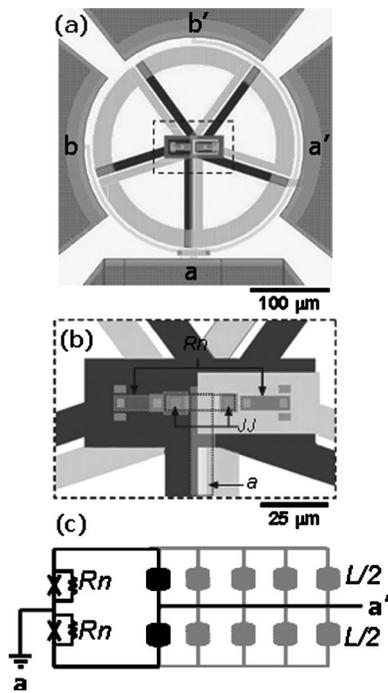
FIG. 2. (a) Layout of our multiloop SQUID design. a and a' are the SQUID terminals and b and b' the contact pads of the integrated feedback coil. (b) Expanded view of the center of the multiloop SQUID. The Josephson junctions are labeled JJ, the shunt resistances R_n, and the SQUID upper contacts a, respectively. The dark and light regions represent the two superconducting layers forming each spoke, which are separated by an insulating layer in crossover regions. (c) Equivalent circuit diagram of the multiloop SQUID. R_n represents the shunt resistance in parallel with the JJ and L is the inductance of each individual spoke (fractional turn). The inductance of the device is inversely proportional to the number of spokes.

nomena. As we have outlined above, the size of the SQUID sensing area cannot be scaled up by using a bare SQUID design. Therefore, in order to overcome these limitations, we used a monolithic low-T_c niobium multiloop, or fractional turn, SQUID design. This approach was implemented by Zimmerman in 1971.[23] Figure 2 shows the sensor layout and equivalent circuit of one of our designs. The multiloop SQUID is comprised of multiple pickup coils connected in parallel, thereby reducing the self-inductance of the SQUID sensor. In this way, the effective sensing area can be increased with little compromise of field sensitivity. Therefore, we have fabricated a series of multiloop SQUID sensors with diameters ranging from 250 μm to 1 mm. For a 250 μm diameter, five-spoke multiloop SQUID, we achieved a flux

noise of 1.7 $\mu\phi_0/\mathrm{Hz}^{1/2}$ with an equivalent field sensitivity of 450 fT/$\mathrm{Hz}^{1/2}$ in the white noise region for frequencies above 100 Hz.[24] For a larger diameter, we increased the number of spokes. Using a 500 μm, six-spoke multiloop SQUID, we achieved a flux noise of 4.4 $\mu\phi_0/\mathrm{Hz}^{1/2}$ with an equivalent field sensitivity of 240 fT/$\mathrm{Hz}^{1/2}$ in the white noise region for frequencies above 100 Hz. The increased field sensitivity of the multiloop SQUID design makes it ideally suited for imaging magnetic fields associated with action current propagation in isolated tissue preparations. In comparison with the 250 μm miniature pickup coils, the field sensitivity is improved by a factor of 2. Furthermore, by reducing the sensing volume to a single plane, we increased our signal-to-noise ratio and our spatial resolution. Table I summarizes the performance of our different sensing configurations.

B. Cryogenic design

The SQUID Dewar provides the cryogenic temperatures and the thermal insulation which allows for operating a low-T_c SQUID in close proximity to a RT sample. A schematic of the SQUID Dewar is shown in Fig. 3. The cryogenic system is based on a commercially available custom-built G-10 fiberglass Dewar (Infrared Laboratories, HDL-8). In order to achieve liquid He and N$_2$ hold times of three days, we used 4.96 l He and 5.88 l N$_2$ reservoirs in our Dewar. The N$_2$ reservoir is stacked over the He reservoir. An aluminum thermal radiation shield is thermally anchored to the N$_2$ reservoir. The radiation shield surrounds the He reservoir and extends to the tail of the Dewar [see Fig. 3 (top)]. The aluminum shielding is wrapped with several layers of aluminized Mylar™ foil. This reduces the radiation load from room temperature, therefore decreasing both the liquid He and N$_2$ consumption. This design results in He and N$_2$ consumption rates of 500 and 1100 sccm, respectively. The consumption rates are monitored for diagnostic purposes during operation using a mass flow meter.

The RT sample and the vacuum space of the Dewar are separated by a 25 μm thick sapphire window. Several scanning SQUID microscope systems, using mainly high-T_c superconducting SQUID sensors, have successfully used this approach for the vacuum window.[18,25–27] Sapphire has a low electrical conductivity, which is critical in order to avoid sources of Johnson noise close to the sensor. It also has a high elastic modulus, which minimizes the inward deflection of the sapphire due to the pressure difference. Furthermore,

TABLE I. Flux noise and field sensitivity of all our SQUID sensor configurations. $S_\phi^{1/2}(f)$ and $S_B^{1/2}(f)$ are the magnetic flux and field noise per unit bandwidth at the specified frequency.

| Sensor configuration	$S\phi^{1/2}$(100 Hz) ($\mu\phi_0/\mathrm{Hz}^{1/2}$)	$S_B^{1/2}$(1 Hz) (pT/$\mathrm{Hz}^{1/2}$)	$S_B^{1/2}$(100 Hz) (pT/$\mathrm{Hz}^{1/2}$)	$S_B^{1/2}$(1 KHz) (pT/$\mathrm{Hz}^{1/2}$)
Bare SQUID, 40 μm washer, 40 μm hole	4.0	3.5	1.52	1.50
Multiloop SQUID, 250 μm diameter, 5 spokes	1.7	2.1	0.48	0.45
Multiloop SQUID, 500 μm diameter, 6 spokes	4.4	1.85	0.28	0.24
Multiloop SQUID, 1 mm diameter, 8 spokes	6.0	0.94	0.18	0.15
Miniature coils, 250 μm diameter, 10 turns	2.0	0.85	0.85	0.85
Miniature coils, 500 μm diameter, 20 turns	2.0	0.33	0.33	0.33
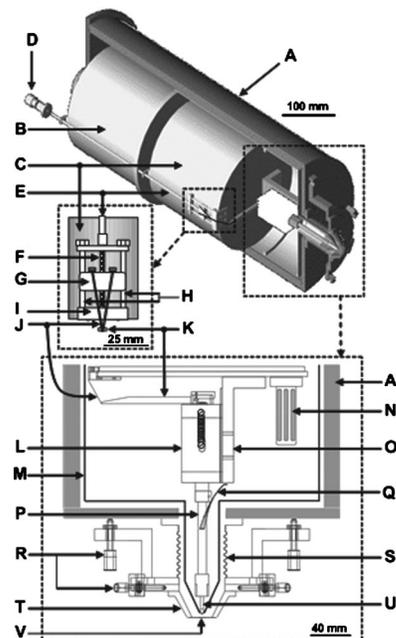
FIG. 3. Detailed cross-sectional schematic of the SQUID microscope Dewar. Top: Cryostat. (A) G-10 fiberglass Dewar casing, (B) liquid N2 reservoir, (C) liquid He reservoir. Middle: Positioning mechanism. (D) Rotary vacuum feed-through, (E) G-10 rod, (F) lead screw, (G) slider, (H) slider posts, (I) brass connection, (J) Kevlar tread, and (K) lever arm. Bottom: SQUID Dewar tail. (L) Aluminum flexure bearing support structure, (M) aluminum thermal radiation shield, (N) cryopump, (O) copper L-shaped bracket, (P) copper cold finger, (Q) flexible copper braids, (R) micrometer positioning screws, (S) brass bellows, (T) G-10 cone, (U) sapphire rod, and (V) 25 mm thick sapphire window.

sapphire has the advantage of being optically transparent, which facilitates the centering and alignment procedure of the sensor with respect the window. A 1 mm thick sapphire backing window with an outer diameter of 25 mm and inner diameter of 1.5 mm supports the 25 μm thin window to minimize bowing. Following the calculations of Lee *et al.*,[25] we have estimated a window bowing on the order of 1 μm.

In order to maintain a good insulation vacuum for longer periods of time and to increase the pumping speeds for water and gases like O_2, N_2, and He, we have incorporated a container filled with activated charcoal, which acts as a cryopump. The container is thermally anchored to the He tank. Figure 3 (bottom) shows its location on the He reservoir.

Our SQUID microscope system can be kept at cryogenic temperatures for periods of over one month without deterioration in performance. During this time range, we performed consecutive 23 h high-resolution magnetic field scans of geological samples during a demagnetization experiment at a sensor-to-sample distance of 120 μm. The scans were interrupted only by the liquid N_2 and He transfers. Therefore, we confirmed the reliability of the instrument to operate under the identical conditions over long periods of time.

C. Cold finger design

SQUID microscopes generally have the position of the sensor or pickup coil fixed and it is necessary to adjust the Dewar tail to bring the window as close as possible to the cold sensor. In our experience, this procedure is cumbersome, because not only the distance has to be adjusted, but also the tilt between the window and the sensor surface. To overcome part of the problem, we have incorporated a flexure bearing mechanism actuated by a lever arm to precisely and easily control the vertical position of the sensor into our system. A cross section of the Dewar tail with the lever mechanism is shown in Fig. 3 (bottom). The cryogenic positioning system consists of three different main components. On the top of the Dewar, a rotary vacuum feed-through is connected to a G-10 rod. The G-10 rod is attached to a lead screw and a slider that converts the screw rotational movement into a vertical displacement. The slider is connected to the lever arm via a Kevlar™ tread [see Fig. 3 (middle)]. The lever arm pushes against a shaft that is mounted in the center of two flexure bearings, which are spaced 50 mm apart and anchored to an aluminum support structure. The cold finger is clamped to the shaft and extends it towards the vacuum window. The two flexure bearings in the support structure provide mechanical stability and ensure precise vertical displacement. We have measured a vertical displacement of about 40 μm per turn of the rotary vacuum feed-through. Using this mechanism, we can precisely control the vertical position of the SQUID sensor with respect to the sapphire window. We generally set the distance between the sensor and the sample by approaching the window until we notice a small increase in the He boil-off rate as measured by a mass flow meter. We then confirm the position of the SQUID with respect to the sapphire window with an inverted optical microscope and adjust the tilt, if necessary, after the cool-down procedure. Using this approach, we found that the distance between the sensor and the sample can be reproducibly adjusted to 100 μm.[22]

The cold finger terminates in a collet that holds a sapphire rod. The collet is tightened using a G10-nut. A thin layer of Apiezon™ grease on the sapphire rod provides a good thermal contact to the copper cold finger. Additional thermal links to the solid copper L-shaped bracket mounted on the He reservoir are provided by two flexible copper braids soldered into the center of the cold finger. Depending on the sensor configuration, the sapphire rod has a bobbin machined at the tip (for miniature pickup coils) or is conical shaped (for monolithic sensor chips).

The monolithic SQUID sensor chips are mounted on the tip of the conical shaped sapphire rod. Using a diamond impregnated wire saw, we first cut the edges of 2.5×2.5 mm^2 chip to reduce its diameter to a few hundred micrometers. This method is very effective in reducing the size of the chip without damaging the gold contact pads that will be used to connect to the SQUID and the integrated feedback line. We then mount the SQUID chip on the tip of the sapphire rod using a low-temperature epoxy resin (Stycast™). After mounting the chip, we grind and polish the edges of the chip to reduce its diameter and to provide a smooth surface around the edge. We deposited 200-nm silver pads to extend the electrical connection around the edges toward the side of the chip. Four 25 μm gold wires are then attached to the silver pads on the sides of the SQUID chip using silver epoxy to connect the SQUID to a cold step-up transformer, the
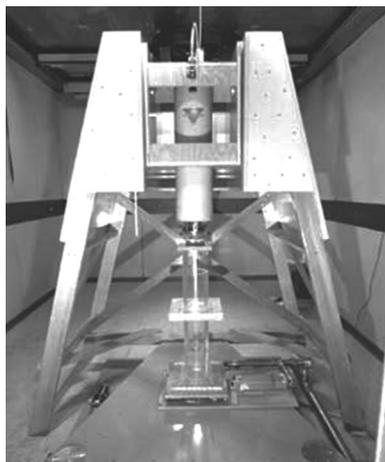
FIG. 4. Photograph of the entire system including a nonmagnetic scanning stage and SQUID Dewar wooden support structure. The SQUID microscope system is housed inside a three-layer μ-metal magnetically shielded room.

dc bias source, and the feedback coil of the flux-locked loop (FLL) electronics.

D. System integration

Figure 4 shows a picture of the entire system. The SQUID microscope Dewar is supported by a wooden structure above the non-magnetic scanning stage. Two high-precision piezoelectric inchworm motors are used to perform the XY-raster scan.[18] The whole system is housed in a three-layer, μ-metal shielded room (Vacuumschmelze, Hanau) to eliminate near-zero and high-frequency background noise. The monolithic dc-SQUID sensors are operated in FLL configuration with custom-designed electronics,[28] which use a flux modulation frequency of 100 KHz. For a high-sensitivity setup, we typically adjust the feedback resistor to provide a dynamic range of $\pm 10\phi_0$, where ϕ_0 is the flux quantum. The output voltage is digitized by a PCI-MIO card (National Instruments) with 16-bit resolution. The stage and acquisition parameters are controlled by software developed using LABVIEW (National Instruments).

III. MEASUREMENTS AND APPLICATIONS

In the following sections, we present applications in two areas where our SQUID microscope system leads to information difficult to obtain with other techniques. As we outlined above, our system can be equipped with different SQUID sensors depending on the particular magnetic source configuration. We first describe applications using SQUID sensors to image magnetic field originating from magnetizations in geological samples, which do not require a compromise between spatial resolution and field sensitivity, provided we can get the sensor close to the sample. Therefore, a monolithic bare SQUID design is the best suited approach. In contrast, when imaging action or injury currents generated by living tissue, the current sources are weak and distributed, requiring sensors with higher sensitivities. In order to achieve these higher sensitivities, we must compromise spatial resolution. The multiloop SQUID sensor is ideal for this application.

A. Paleomagnetism

One of the major research areas that will benefit from the development of our SQUID microscopes is paleo- and geomagnetism. Kirschvink argued that the many paleomagnetic studies were limited by the sensitivity of current magnetometer systems in use.[29] He showed that magnetizations at the level of 10^{-14} to 10^{-15} A m^2 can be preserved in sedimentary rocks. Current commercially available magnetometers like the 2G superconducting rock magnetometer have moment sensitivities around 10^{-12} A m^2. The sensitivity of our SQUID microscope system can also be expressed as moment sensitivity. For our bare SQUID design with an effective diameter of 80 μm, we calculated a magnetic moment sensitivity of 5.4×10^{-18} A m^2/Hz$^{1/2}$ for frequencies above 100 Hz at a sensor-to-sample spacing of 100 μm.

Superconducting rock magnetometers measure the average magnetization in a sensing volume of a 1 in. round and 1 in. high cylinder. In contrast, SQUID microscopy provides images of the magnetic field above the sample with submillimeter resolution. This is especially important for geological samples that are not homogeneously magnetized. We can now study the geomagnetic properties on a grain-by-grain basis in integral geological samples in massively parallel measurements. This results in information which is difficult or impossible to obtain using conventional superconducting rock magnetometers.

Using our first generation SQUID microscope with a 250 μm pickup coil, we imaged the magnetic field associated with the remanent magnetization of the Martian meteorite ALH84001. We performed a thermal demagnetization experiment to determine the maximum temperature the rock has been exposed to since ejected from Mars through a meteoroid impact.[15,16] Since then, we have improved the SQUID microscope, and incorporated our monolithic bare SQUID sensors, which drastically improved the field sensitivity and spatial resolution of the system. Figure 5 shows a direct comparison between images obtained with a 250 μm pickup coil and a bare SQUID washer design with an effective diameter of 120 μm. The images show magnetic field distributions resulting from the remanent magnetization of a 30 μm thin section of a basalt pillow from the Kilauea Volcano, Hawaii at a sample-to-sensor distance of 120 μm. In order to show the improvement in spatial resolution, we took a line scan along identical features at the same location in both magnetic images [see Fig. 5(d)]. The dashed line is from the scan measured with the 250 μm pickup coil and the solid line from the bare SQUID with an effective diameter of 120 μm. We can clearly identify smaller features on the order of the effective diameter of the monolithic SQUID sensor, which are averaged in images obtained with the 250 μm pickup coil. The spatial averaging has both contributions from the larger diameter and the volume of the pickup coil.

Many paleomagnetic techniques require successive recordings of the magnetic field of the sample after demagnetization or remagnetization experiments. For these experiments it is essential to spatially correlate the magnetic field maps after each recording, which requires the sample to be registered with respect to the sensor height and the scanning directions. To address this issue, we developed a spring-
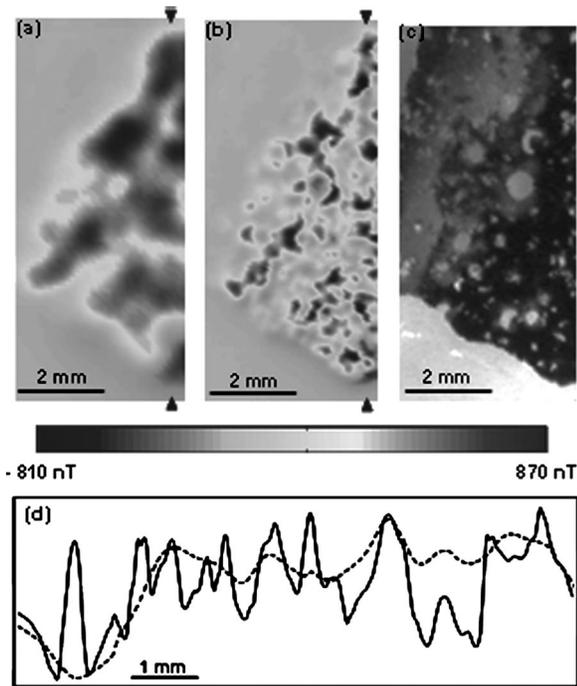
FIG. 5. Comparative magnetic field maps of a 30 μm thin section of a basalt pillow recorded using (a) a hand-wound nine-turns 250 μm diameter pick-up coil inductively coupled to a commercial SQUID sensor. (b) Bare SQUID design with an effective diameter of 120 μm. (c) Optical picture of the imaged area. (d) Line scans through both magnetic field images at identical locations as indicated by arrows in (a) and (b). The dashed line corresponds to image (a) and the solid line to image (b).

loaded mechanism attached to the scanning stage, which allows us to scan a flat thin section in contact with the sapphire window. Figure 6 shows a schematic of the mechanism. A rectangular Plexiglas™ sample holder sits over a pair of rubber bands and fits tightly inside a square opening. The mechanism is mounted on top of the pedestal of our scanning stage. In this way, we scan a flat sample in contact with the window and guarantee that the sample will be as close as possible to the sensor. This setup allows us to remove the sample, perform alternating field demagnetization or isothermal remanent magnetization steps on the sample, and place it in the same location to correlate measurements and identify the underlying petrography.
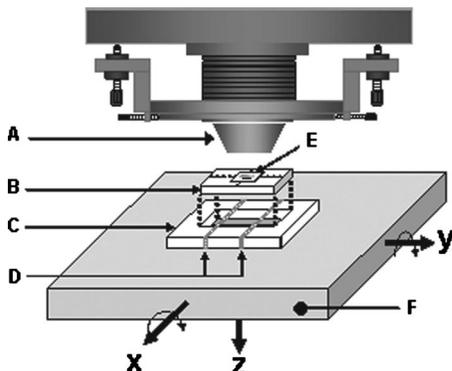

FIG. 6. Schematic of spring-loaded mechanism mounted on the top of the scanning stage. (A) Tail of the SQUID microscope, (B) sample holder, (C) support frame, (D) rubber bands, (E) geological thin section (sample), and (F) Plexiglas pedestal attached to base of the scanning stage.
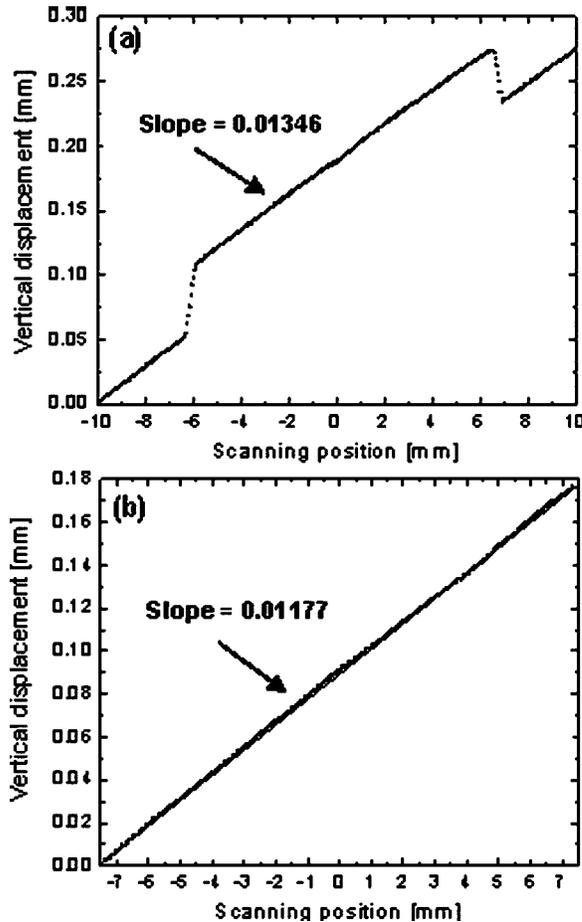

FIG. 7. (a) Relative height between the scanning stage platform and the vacuum window of the SQUID microscope during a line scan. The steps in the curve result from the thickness of the 25 μm sapphire window and a thin layer of epoxy used to glue the sapphire window to the backing window. (b) Vertical displacement of the sample holder while pressed against the window by the spring-loading mechanism during a line scan. From these measurements, we estimated a tilt of 0.097° between the sample surface and the sapphire window.

To test the precision of the spring-loaded mechanism, we used a 1 μm precision dial indicator to measure the relative tilt between the surface of the window and a flat sample while scanning. Figure 7 shows this measurement. First, we measured the relative tilt between the scanning stage and the window [Fig. 7(a)]. The two steps in the scan are caused by the thickness of the thin sapphire window with a thin layer of epoxy. We then placed the dial indicator below the sample holder in order to measure the tilt of the holder while scanning against the window [Fig. 7(b)]. Comparing these two measurements, we estimated a relative tilt between the surface of the window and the sample holder of 0.097° while performing a scan.

To register the magnetic field images and correlate them to petrography or a compositional analysis we have developed a spatial registration technique. Figure 8 shows an example of the method for a geological thin section. After the sample's magnetic distribution has been acquired, we remove the sample and place a wire in a cross-hair pattern in its place. We then apply an alternating current through the wire and measure its magnetic field pattern using a lock-in amplifier technique over the same area where the sample was
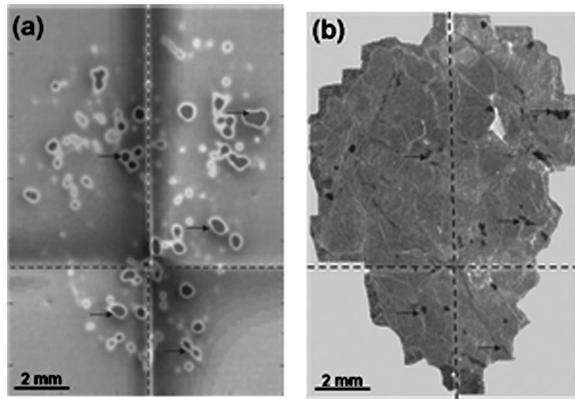
FIG. 8. (a) Superposition of the magnetic field map from the sample and the magnetic field generated by wires across the sample used for registration purposes. (b) Optical picture of the sample. The dashed line shows the position of the wire. This registration technique allows us to correlate magnetic features with features in the optical image (arrows).
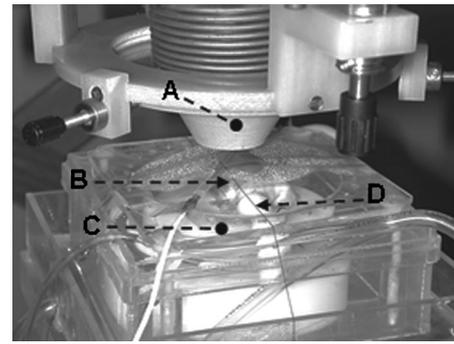

FIG. 9. Photograph of the experimental setup to record the magnetocardiogram on the surface of an isolated rabbit heart. (A) Tail of the SQUID microscope, (B) isolated rabbit heart, (C) tissue bath, and (D) registration wires.

located. From the wire magnetic mapping, we can localize the position of the wire by the zero-field crossing. Since both the sample and the wire scan were measured with respect to the same origin defined by the coordinate system of the scanning stage, we can now spatially superimpose these two images. We then take an optical image of the wire pattern and the sample for angular alignment. Using a scale bar, we can then adjust the size of the optical image to the magnetic image that was taken using the reference coordinate system of the scanning stage. Using this technique, we can overlap and correlate specific features in the magnetic images with the location in the optical image. This registration technique could also be used for a correlation to a compositional or crystallographic analysis.

Our sample-to-sensor spacing of around 100 μm limits both our spatial resolution to 100 μm and our moment sensitivity to 10^{-18} Am^2/Hz$^{1/2}$ in the white noise region for frequencies above 1 Hz. We are currently working to reduce both the sample-to-sensor spacing and the sensor size. We expect to improve our spatial resolution by at least a factor of 2 and, consequently, our moment sensitivity by a factor of 8.

A great variety of geo- and paleomagnetic experiments can now be done on individual grains in standard petrographic thin sections and the measured magnetic field can be matched to the composition and to the petrography of the sample. The incorporation of monolithic bare SQUID sensors into our scanning SQUID microscope allows measurements currently not possible with existing commercially available instrumentation.

B. Biomagnetism

SQUID magnetometer systems have been widely used to study a great variety of bioelectric and biomagnetic phenomena.[12] Multichannel SQUID systems with pickup coil diameters of 10 to 30 mm with a similar sample-to-sensor spacing are generally used in human studies. These systems do not provide the spatial resolution necessary to study the generation of the magnetic activity or injury currents at tissue and cellular scales. In excitable tissue extracellular potentials, transmembrane potentials, or action cur-

rents are interrelated. To make model predictions, one should at least measure more than one of these quantities, especially in tissues with different anisotropies in the intra- and extracellular space. The extracellular potentials are typically recorded using microneedle arrays. However, the insertion of microneedles influences the measurement results[30] and is impractical to achieve submillimeter spatial resolution. Our approach is to record the transmembrane potential optically and the action currents using SQUID microscopy, which allows us to obtain more detailed information on the generation of the magnetocardiogram (MCG). High-resolution biomagnetic imaging provides insights that will improve existing mathematical models of biological tissue.

By using a six-spoke 500 μm diameter multiloop SQUID, we recorded MCGs on the surface of a perfused isolated rabbit heart. Figure 9 shows a photograph of a perfused isolated rabbit heart in a tissue bath under the tail of the Dewar. A bath temperature of 38 °C is maintained by a second perfusion system and a heat exchanger. The heart was stimulated at a frequency of 3.33 Hz using a single coaxial electrode placed on the posterior left ventricular (LV) wall. The amplitude of the stimulation pulse was 2 mA, which is just above the threshold for diastolic stimulation. The anterior depolarization wave fronts generated by the stimulation pulse were imaged using a membrane bound fluorescent dye and a high-speed CCD camera.[31] After recording the transmembrane potential optically, the isolated rabbit heart was positioned under the tail of the SQUID microscope and lightly pressed against the sapphire window to minimize the sample-to-sensor spacing. One-second-long time traces of the magnetic field generated by the excitation were recorded at 144 locations on a 12 mm $\times$ 12 mm grid with a step size of 1 mm. The data acquisition was triggered on the stimulation pulse, allowing for synchronization of the magnetic field traces to produce a time series of two-dimensional field maps.

Figure 10(a) depicts the areas for the optical (blue) and the magnetic (red) recordings in relation to the anatomical features of the isolated heart. Time traces of the transmembrane potential and the magnetic field at the marked location are shown in Fig. 10(b). An optical image of the propagating depolarization wave front 53 ms after stimulation can be seen in Fig. 10(c). The optical data are offset by the resting
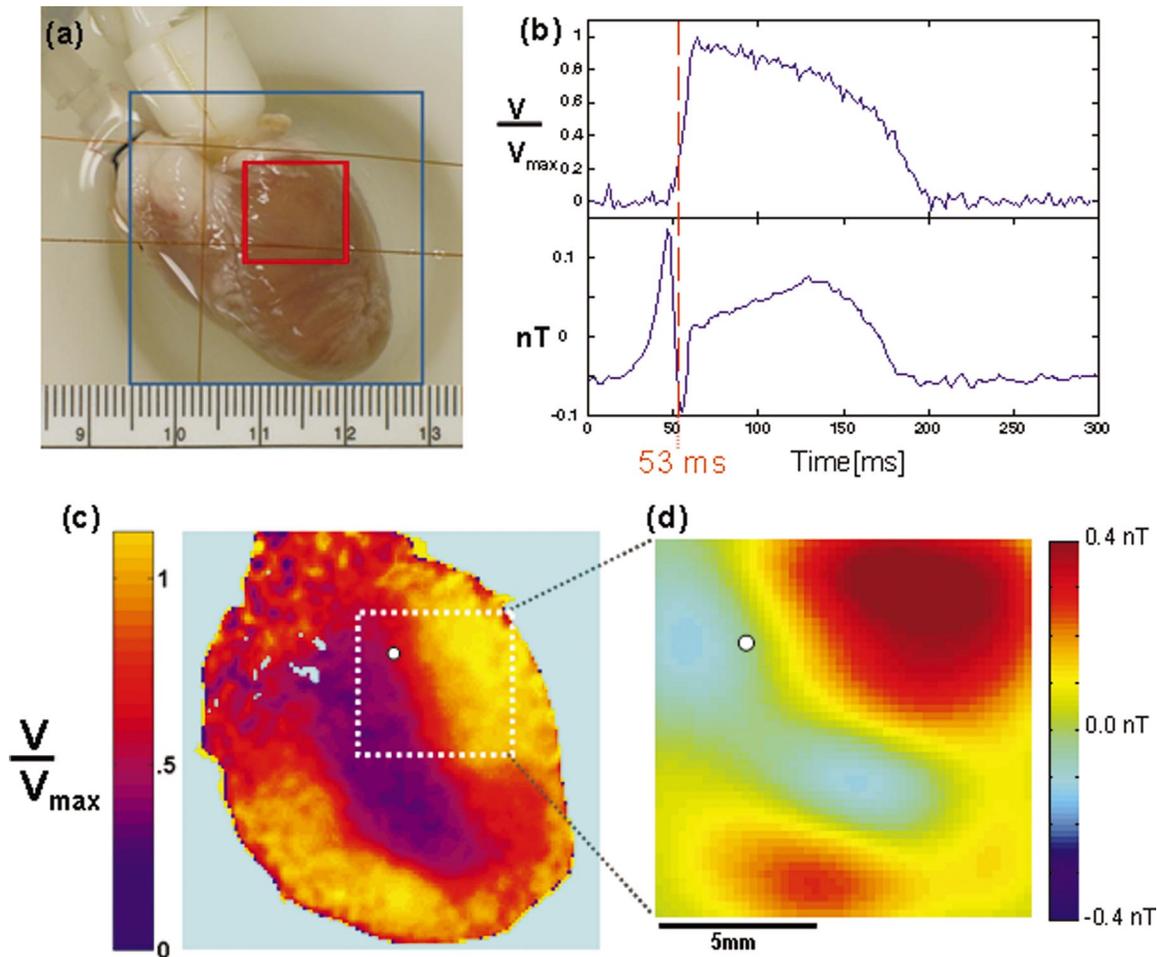
FIG. 10. (Color) (a) Optical image of a Langendorff perfused rabbit heart indicating the imaging areas used to record transmembrane potentials (blue square) and magnetic fields (red square) associated with action currents. (b) Time trace of the transmembrane potential and the magnetic field recorded from the same location on the surface of the heart. (c) Image of the transmembrane potential distribution 53 ms after stimulation. The two wave fronts from opposite sides are about to collide. (d) Magnetic field image composed of time traces 53 ms after the stimulus from the area indicated by a white dashed square in (c).

potential and normalized by the maximum amplitude of the transmembrane potential. The wave fronts can be identified as the boarder between depolarized ($V/V_{max} \sim 1$) and resting tissue ($V/V_{max} \sim 0$). As shown in the image, two wave fronts originating from the posterior point stimulus are about to collide. A magnetic field map of an area on the LV, as marked by the white square in Fig. 10(c), is shown in Fig. 10(d).

In a previous study, we used a line stimulus in close proximity to the imaging area to generate a plane wave. We found that a reversal of magnetic field polarity is associated with the depolarization wave front.[7] The data presented here show that the wave front geometry cannot be accurately predicted by a contour line between areas of opposite field polarity. This suggests that action currents flow over larger distances and, therefore, the wave fronts influence each other over larger distances than suggested by the depolarization contours of the transmembrane potential maps.

It is clear from our observations that the intra- and interstitial potentials, and, therefore, the currents are not scaled versions of the local transmembrane potential. The currents are determined by the transmembrane potential throughout the tissue and a local description in terms of a generator model is not applicable.[32,33] A detailed analysis of the data, a reduction in dimensionality to reduce the influence of fiber orientation, and well-defined wave front geometries are required to make more precise model predictions.

The improvement in field sensitivity achieved by using monolithic multiloop SQUID sensors allows us to study in more detail the relationship between extracellular potentials, transmembrane potentials, and action currents, especially in thin layers of connective cardiac or brain tissue. We hope to achieve a higher sensitivity by optimizing the process parameters to lower the critical currents of the Josephson junction of our multiloop SQUID sensors. For an optimized 1 mm multiloop SQUID sensor, we expect to achieve field sensitivities on the order of 20 fT/Hz$^{1/2}$.

ACKNOWLEDGMENTS

[1] J. R. Kirtley and J. P. Wikswo, Jr., Annu. Rev. Mater. Sci. **29**, 117 (1999).

[2] J. R. Kirtley, Physica C **368**, 55 (2002).

[3] J. P. Wikswo, *SQUID Sensors: Fundamentals, Fabrication and Applications*, edited by H. Weinstock (Kluwer Academic, Dordrecht, 1996), p. 307.

[4] I. M. Thomas, S. M. Freake, S. J. Swithenby, and J. P. Wikswo, Phys. Med. Biol. **38**, 1311 (1993).

[5] Y. R. Chemla, H. L. Grossman, T. S. Lee, J. Clarke, M. Adamkiewicz, and B. B. Buchanan, Biophys. J. **76**, 3323 (1999).

[6] F. Baudenbacher, N. T. Peters, P. Baudenbacher, and J. P. Wikswo, Physica C **368**, 24 (2002).

[7] J. R. Holzer, L. E. Fong, V. Y. Sidorov, J. P. Wikswo, and F. Baudenbacher, Biophys. J. **87**, 4326 (2004).

[8] F. Baudenbacher, L. E. Fong, G. Thiel, M. Wacke, V. Jazbinsek, J. R. Holzer, A. Stampfl, and Z. Trontelj, Biophys. J. **88**, 690 (2005).

[9] S. Chatraphorn, E. F. Fleet, F. C. Wellstood, L. A. Knauss, and T. M. Eiles, Appl. Phys. Lett. **76**, 2304 (2000).

[10] E. F. Fleet, S. Chatraphorn, F. C. Wellstood, and L. A. Knauss, IEEE Trans. Appl. Supercond. **9**, 4103 (1999).

[11] H. Weinstock, IEEE Trans. Magn. **27**, 3231 (1991).

[12] J. P. Wikswo, Jr., *Applications of Superconductivity*, edited by H. Weinstock (Kluwer Academic, Dordrecht, 2000), p. 139.

[13] U. Klein, M. E. Walker, C. Carr, D. M. McKirdy, C. M. Pegrum, G. B. Donaldson, A. Cochran, and H. Nakane, IEEE Trans. Appl. Supercond. **7**, 3037 (1997).

[14] A. Abedi, J. J. Fellenstein, A. J. Lucas, and J. P. Wikswo, Rev. Sci. Instrum. **70**, 4640 (1999).

[15] B. P. Weiss, H. Vali, F. J. Baudenbacher, J. L. Kirschvink, S. T. Stewart, and D. L. Shuster, Earth Planet. Sci. Lett. **201**, 449 (2002).

[16] B. P. Weiss, J. L. Kirschvink, F. J. Baudenbacher, H. Vali, N. T. Peters, F. A. Macdonald, and J. P. Wikswo, Science **290**, 791 (2000).

[17] B. J. Roth, N. G. Sepulveda, and J. P. Wikswo, Jr., J. Appl. Phys. **65**, 361 (1989).

[18] F. Baudenbacher, N. T. Peters, and J. P. Wikswo, Jr., Rev. Sci. Instrum. **73**, 1247 (2002).

[19] B. P. Weiss, F. J. Baudenbacher, J. P. Wikswo, and J. L. Kirschvink, EOS Trans. Am. Geophys. Union **82**, 513 (2001).

[20] C. D. Tesche and J. Clarke, J. Low Temp. Phys. **29**, 301 (1977).

[21] J. M. Jaycox and M. B. Ketchen, IEEE Trans. Magn. **17**, 400 (1981).

[22] F. Baudenbacher, L. E. Fong, J. R. Holzer, and M. Radparvar, Appl. Phys. Lett. **82**, 3487 (2003).

[23] J. E. Zimmerman, J. Appl. Phys. **42**, 4483 (1971).

[24] L. E. Fong, J. R. Holzer, K. McBride, E. A. Lima, F. Baudenbacher, and M. Radparvar, Appl. Phys. Lett. **84**, 3190 (2004).

[25] T. S. Lee, E. Dantsker, and J. Clarke, Rev. Sci. Instrum. **67**, 4208 (1996).

[26] F. Gruhl, M. Muck, M. von Kreutzbruck, and J. Dechert, Rev. Sci. Instrum. **72**, 2090 (2001).

[27] R. C. Black, Ph.D. thesis, University of Maryland, 1995.

[28] J. Clarke, W. M. Goubau, and M. B. Ketchen, J. Low Temp. Phys. **25**, 99 (1976).

[29] J. L. Kirschvink, *SQUID Applications to Geophysics*, edited by H. Weinstock (Kluwer Academic, Dordrecht, 1981), p. 111.

[30] D. M. Langrill and B. J. Roth, IEEE Trans. Biomed. Eng. **48**, 1207 (2001).

[31] S.-F. Lin, R. A. Abbas, and J. P. Wikswo, Jr., Rev. Sci. Instrum. **68**, 213 (1997).

[32] R. Plonsey and R. C. Barr, Biophys. J. **45**, 557 (1984).

[33] R. Plonsey and Y. Rudy, Med. Biol. Eng. Comput. **18**, 87 (1980).